Extensive Broadband X-Ray Monitoring During the Formation of a Giant Radio Jet Base in Cyg X-3 with *AstroSat*

Mayukh Pahari[1,2] ⓘ, J S Yadav[2], Jai Verdhan Chauhan[2] ⓘ, Divya Rawat[3], Ranjeev Misra[1], P C Agrawal[4], Sunil Chandra[2,5] ⓘ, Kalyani Bagri[6], Pankaj Jain[3], R K Manchanda[7], Varsha Chitnis[8], and Sudip Bhattacharyya[2] ⓘ
[1] Inter-University Center for Astronomy and Astrophysics, Ganeshkhind, Pune 411007, India; mayukh@iucaa.in
[2] Department of Astronomy and Astrophysics, Tata Institute of Fundamental Research, Colaba, Mumbai 400005, India
[3] Department of Physics, IIT Kanpur, Kanpur, Uttar Pradesh 208016, India
[4] UM-DAE Centre for Excellence in Basic Sciences, University of Mumbai, Kalina, Mumbai, Maharashtra 400098, India
[5] School of Physical and Chemical Sciences, North-West University, Potchefstroom 2520, South Africa
[6] School of Studies in Physics and Astrophysics, Pt. Ravishankar Shukla University, Raipur, Chhattisgarh 492010, India
[7] University of Mumbai, Kalina, Mumbai 400098, India
[8] Department of High Energy Physics, Tata Institute of Fundamental Research, Colaba, Mumbai 400005, India
Received 2017 November 19; revised 2018 January 8; accepted 2018 January 8; published 2018 January 19

Abstract

We present X-ray spectral and timing behavior of Cyg X-3 as observed by *AstroSat* during the onset of a giant radio flare on 2017 April 1–2. Within a timescale of a few hours, the source shows a transition from the hypersoft state (HPS) to a more luminous state (we termed as the very high state), which coincides with the time of the steep rise in radio flux density by an order of magnitude. Modeling the Soft X-ray Telescope (SXT) and Large Area X-ray Proportional Counter (LAXPC) spectra jointly in 0.5–70.0 keV, we found that the first few hours of the observation is dominated by the HPS with no significant counts above 17 keV. Later, an additional flat power-law component suddenly appeared in the spectra that extends to very high energies with the power-law photon index of $1.49^{+0.04}_{-0.03}$. Such a flat power-law component has never been reported from Cyg X-3. Interestingly the fitted power-law model in 25–70 keV, when extrapolated to the radio frequency, predicts the radio flux density to be consistent with the trend measured from the RATAN-600 telescope at 11.2 GHz. This provides direct evidence of the synchrotron origin of flat X-ray power-law component and the most extensive monitoring of the broadband X-ray behavior at the moment of decoupling the giant radio jet base from the compact object in Cyg X-3. Using SXT and LAXPC observations, we determine the giant flare ejection time as MJD 57845.34 ± 0.08 when 11.2 GHz radio flux density increases from ∼100 to ∼478 mJy.

Key words: accretion, accretion disks – black hole physics – X-rays: binaries – X-rays: individual (Cyg X-3)

1. Introduction

Establishing the true nature of the connection between the accretion disk and radio jets in X-ray binaries at different mass accretion rate has been considered one of the challenging problems in astrophysics and several attempts have been made so far in this direction (Fender et al. 2004, 2009; Dinçer et al. 2014). Such attempts successfully establish the long-term radio/X-ray correlations from weeks to years timescales in both transient and persistent/semi-persistent sources like GX 339-4 (Corbel et al. 2013), Cyg X-1 (Stirling et al. 2001), GRS 1915+105 (Muno et al. 2001; Fender & Belloni 2004), and Cyg X-3 (Zdziarski et al. 2016). However, there are a handful of attempts where inner disk activity was closely monitored before, during, and after the superluminal radio ejection from X-ray transients. Miller-Jones et al. (2012) made a remarkable attempt during the 2009 outburst of the Galactic micro-quasar H 1743-322. They monitored the formation and ejection of superluminal radio jets using VLBA at 8.4 GHz between 2009 May 28 and June 6 almost on a daily basis simultaneously with the *RXTE*/PCA observations to monitor accretion flow properties. They found that radio emission was highly quenched before the major radio flare and the ejection event occurred during the state transition from hard-intermediate to soft state, which is marked by the disappearance of type-C quasi-periodic oscillations (QPOs) from the power density spectra (Casella et al. 2005). Until now, the changes in X-ray spectro-temporal properties during the formation of a superluminal jet have been monitored with the frequency of days to weeks, except GRS 1915+105, which is only source that has radio and sensitive X-ray data on a scale of days (Yadav 2006). However, depending upon the size of the radio jet base, it is possible that the decoupling may occur in the first few minutes to hours and may leave a signature in X-ray spectro-timing properties. Unfortunately, no studies exist where the change in X-ray properties of the inner accretion flow are traced with the accuracy of a timescale of minutes. One key reason for the lack of such studies is that superluminal radio ejections are rare, transient, and their time of occurrences are completely unpredictable within a timescale of days to weeks. Although a few studies with microquasars have shown that major radio flares occur during the transition from the hard-intermediate to the soft spectral state (Fender et al. 2009), the occurrence of such a transition is highly uncertain within a timescale of weeks. Therefore, it is difficult to determine the time of radio jet formation more accurately than a few days.

Cyg X-3 is a Galactic, high-mass, wind-fed X-ray binary (Parsignault et al. 1972), and on many occasions it shows unique giant radio flares with the peak radio flux density up to 20 Jy (Leach et al. 1975; Molnar et al. 1988; Schalinski et al. 1995; Mioduszewski et al. 2001). Additionally, radio and X-ray variability have been observed from this source, and their correlation has been studied (Zdziarski et al. 2016). Based on hardness and X-ray and radio flux, five X-ray spectral states have been identified (Koljonen et al. 2010): hypersoft state (HPS), flaring soft X-ray state (FSXR), flaring intermediate

state, flaring hard X-ray state, and quiescent state. QPOs of the order of mHz are detected from Cyg X-3 during the hard state (Manchanda & Rao 1993; Koljonen et al. 2011; Pahari et al. 2017). The latest giant radio flare, which reached nearly 20 Jy on 2017 April 4–5, was first predicted by Trushkin et al. (2017b). Monitoring Cyg X-3 using RATAN-600 radio telescope in three bands: 4.6, 8.2, and 11.2 GHz on a daily basis and comparing the *Swift*/BAT hard X-ray flux, they showed that before the giant flare, the source entered into the HPS where both hard X-ray and radio flux are highly quenched (Koljonen et al. 2017). On 2017 April 1–2, the radio flux started increasing rapidly, and on April 4–5 it reached the peak value of ∼20 Jy in all three radio bands. During this period, 15–50 keV *Swift*/BAT flux increased by a factor of ∼2–3. A similar transition from the ultrasoft to the hard X-ray state was also observed previously with *INTEGRAL* (Beckmann et al. 2007). Interestingly, *AstroSat* observed the source continuously on April 1–2 when the X-ray state transition and major radio flare formation were taking place.

In this work, we analyze the simultaneous observations of Cyg X-3 using the Soft X-ray Telescope (SXT) and Large Area X-ray Proportional Counter (LAXPC) instruments on board *AstroSat*. Based on light curve, hardness, and broadband energy spectra, we found that during the first 10–12 hr, the source was in the HPS. After ∼50 ks, an unusual, flat power-law component appeared in the spectrum of Cyg X-3, and we termed it as the very high state (VHS). We show that the flat power-law component is consistent with the synchrotron emission from the radio jet monitored simultaneously with the RATAN telescope. This observation provides an opportunity to closely monitor the X-ray properties during the formation of giant radio flare in Cyg X-3.

2. Observations and Analysis

AstroSat continuously observed Cyg X-3 between 2017 April 1 14:47:24 and 2017 April 2 16:43:39, covering 14 consecutive satellite orbits. The total observation duration is 93.3 ks. For broadband spectroscopic purpose, we use simultaneous observations from the SXT and LAXPC instruments.

SXT is a focusing telescope with a CCD camera that can perform X-ray imaging and spectroscopy in the 0.3–8.0 keV energy range (Singh et al. 2014). Level 1 imaging mode data are processed through a pipeline software to produce level 2 event files and then a good time interval correcter and SXT event merger script[9] is used to create merged event files from all the clean events with the corrected exposure time. We use XSELECT V2.4d in HEASOFT 6.22.1 to extract light curves and spectra using source regions between 1 and 13 arcmin. An off-axis auxiliary response file (ARF) appropriate for the source location on the CCD is generated from the provided on-axis ARF using `sxtmkarf` tool (see footnote 9). Blank-sky SXT observations are used to extract background spectrum.

LAXPC consists of three identical X-ray proportional counters with the absolute time resolution of 10 μs in the energy range 3.0–80.0 keV (Misra et al. 2016; Yadav et al. 2016a, 2016b; Agrawal et al. 2017; Antia et al. 2017). LAXPC data are analyzed using the LAXPC software.[10] Details of the response and background spectra generation can be found in Antia et al. (2017).

In the top left panel of Figure 1, we show the *Swift*/BAT daily light curve in 15–50 keV where the *AstroSat* observation span is marked by two vertical lines. The light curve shows that the *Swift*/BAT count rate sharply rises by a factor of ∼2 within the *AstroSat* observation period. The bottom panel shows the 11.2 GHz radio light curve obtained from the RATAN-600 telescope (Trushkin et al. 2017a). The radio flux density was at a low, persistent level of ∼50–100 mJy until MJD 57845 and then it rises to ∼1 Jy within the *AstroSat* observation window. Therefore, the *AstroSat* observation during the onset of the giant radio flare simultaneous with the X-ray hardening is extremely valuable to monitor the disk/jet connections.

The 3–80 keV background-subtracted LAXPC light curve and 0.3–8 keV SXT light curve are shown in the top right panel of Figure 1. We note that the peak count rate of the binary modulation of ∼4.8 hr observed from both LAXPC and SXT light curves increases significantly (∼50%) after ∼60 ks. To check the soft and hard X-ray behavior of the source, we plot the 3–10 keV, 17–60 keV background-subtracted light curves and their ratios in the bottom left panel of Figure 1. With the 5% background systematics, the source count rate in the 17–60 keV energy range is close to the non-detection level up to ∼60 ks and then increases significantly up to ∼150 counts s^{-1}. Additionally, the hard-to-soft ratio becomes significant after ∼60 ks. This implies the absence of a hard component in the spectra during the first 60 ks. This part of the observation belongs to the HPS. The hard component appears from 60 ks onward during VHS. We check the flux–flux plot in 3–6 keV and 15–60 keV using LAXPC10 observations shown in the bottom right panel of Figure 1. During the HPS, the 3–6 keV count rate strongly correlates with the 15–60 keV count rate with the Spearman rank correlation coefficient (SRCC) of 0.82 (two-tailed *p*-value is <0.0000004), while both light curves are not correlated during the VHS with the SRCC of 0.17 (two-tailed *p*-value is ∼0.0006). The non-correlation indicates that the origin of hard and soft X-ray emission during the VHS may be independent of each other.

To examine the source variability, we plot the soft color (the ratio of count rate between 6–10 keV and 3–6 keV) and the hard color (the ratio of count rate in 10–40 keV and 3–10 keV) as a function of time in the left panel of Figure 2. The modulations in the timescale of the binary orbital period is seen in both soft and hard colors during the HPS and VHS. We confirm this by phase folding the data over the binary orbital period. The hardness intensity diagram (HID) plotted in the right panel of Figure 2 shows that the second half of the observation (shown in red) is significantly harder and brighter than the first half (shown in black), which motivates naming it as "VHS." For comparison, we also plot the HID of the FSXR (in blue), which was observed by *AstroSat* on 2016 August 12.

3. Spectral Analysis and Results

To confirm the HPS to VHS transition as indicated by the model-independent approach, we separately fit SXT+LAXPC joint spectra in the energy range 0.6–70.0 keV extracted during the first 40 ks (HPS) and last 40 ks (VHS). We use the `diskbb` model to fit the HPS emission (Koljonen et al. 2010). However, the disk is embedded in a plasma medium (Manchanda 2002; Zdziarski et al. 2010) accreted from the companion, and
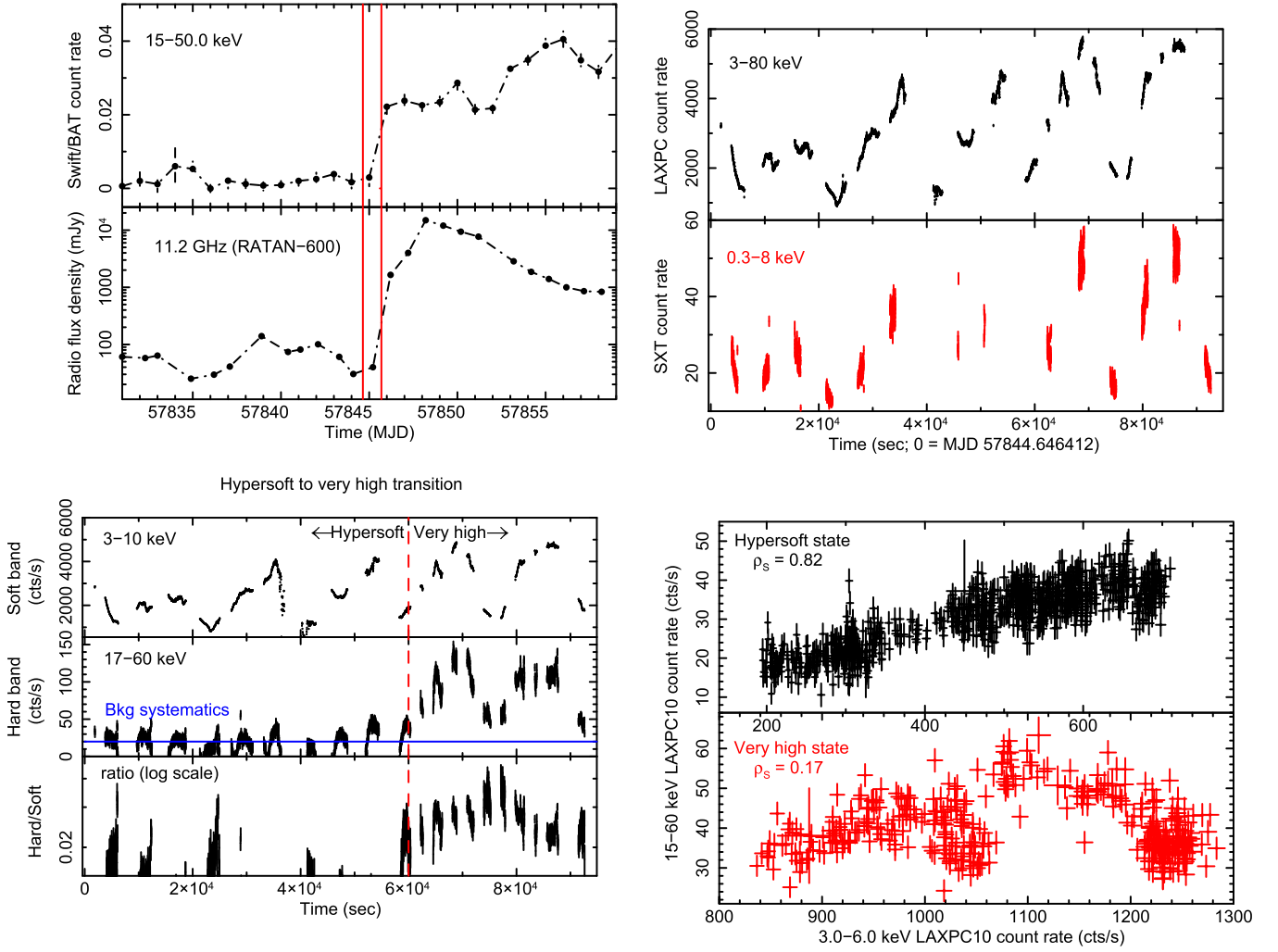

Figure 1. Top left panel shows *Swift*/BAT light curve of Cyg X-3 in the 15–50 keV (top) and simultaneous RATAN-600 radio light curve (bottom) at 11.2 GHz (adopted from Trushkin et al. 2017a, 2017b). The time interval between two vertical red lines is the observation period of *AstroSat*. During this period, the top right panel shows 3–80 keV background-subtracted LAXPC light curve combining all three units (top) and 0.3–8 keV SXT light curve (bottom). For clarity, a 10 s bin time is used. Bottom left panel shows the background-subtracted LAXPC light curve in 3–10 keV (top), 17–60 keV (middle), and their ratio. The dashed vertical line separate two spectral states: hypersoft and very high. The blue horizontal line marks the 5% systematics errors on the estimated background. Bottom right panel shows a flux–flux plot between 3–6 keV and 15–60 keV during the hypersoft (top) and the very high (bottom) state where ρ_s denotes the Spearman rank correlation coefficient.

therefore the bremsstrahlung emission from the collision between the inflowing and outflowing plasma (Koljonen et al. 2013) has been taken care of by the `bremss` model. To account for the interstellar medium absorption and the local, partial absorption by the accreted wind and hot medium, we use `tbabs` and `pcfabs` models, respectively (Koljonen et al. 2010). Fitting with this continuum model, we found weak/no residuals above 20 keV in the HPS but a strong residual in the VHS that resembles a power-law-like emission. To account for this hard X-ray residual, we use the `power-law` model in `XSpec`. The Fe emission line and an absorption feature are modeled using a `Gauss` and a `gabs` model, respectively. Best-fit parameters along with 1σ errors are provided in Table 1. Best-fit spectra during the HPS and the VHS along with their model components and residuals are shown in the top left and top right panels of Figure 3. In the bottom left panel, we plot source+background and background spectra during the VHS in 10–60 keV to show that the flat power-law-like emission observed in the VHS is due to the source only. From Table 1, we note that during the VHS, the hard X-ray excess has a photon power-law index of $1.43^{+0.06}_{-0.03}$. Properties of such a flat power law were not reported from any spectral states in Cyg X-3 and are unlikely to be associated with the coronal emission. To make this point clear, we plot the energy spectra of the FSXR state (in gray) along with the best-fit HPS (shown by pluses) and VHS (shown by circles) in the bottom right panel of Figure 3. Comparing three spectra, we note that the FSXR spectrum has a very distinct and clear coronal emission component in the energy range 10–60 keV which is absent from the HPS and VHS. While the FSXR spectral fitting details will be discussed elsewhere, here it is used for comparison purposes. Since the time of giant radio flare formation coincides with the VHS, the most likely origin of the flat power-law component is the synchrotron emission from the jet base.

3.1. Consistency Check on the Radio Flux Density from the X-Ray Spectra

If the synchrotron emission from the radio jet is the origin of the flat X-ray power law, then an extrapolation of this power
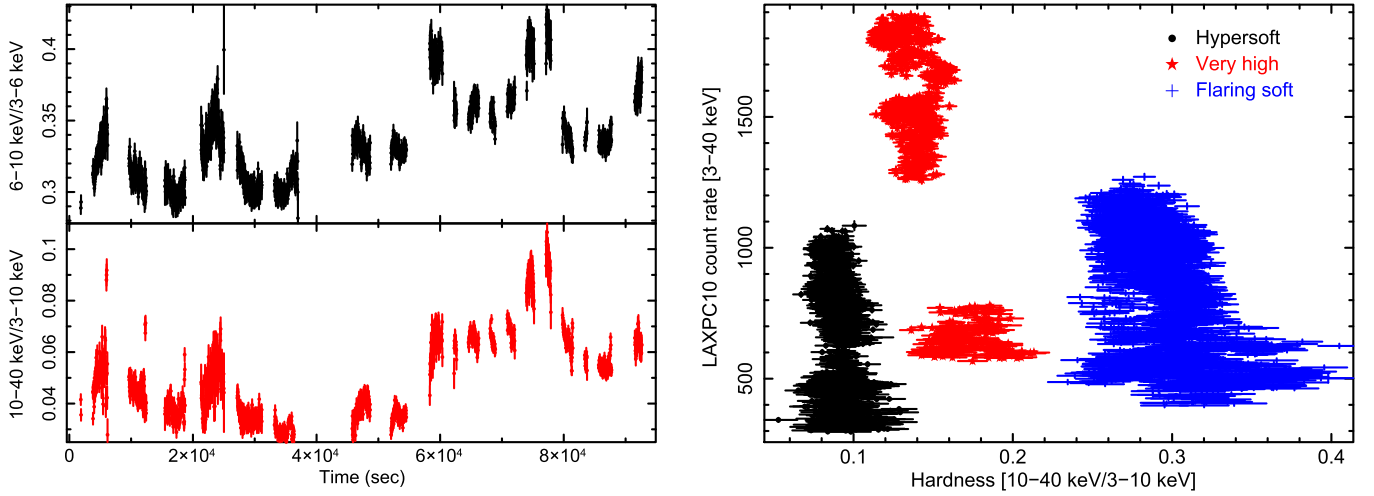
Figure 2. Top left and bottom left panels show the soft color (ratio of count rate in 6–10 keV and 3–6 keV) and the hard color (ratio of count rate in 10–40 keV and 3–10 keV) as a function of time. Right panel shows the hardness intensity diagram (HID) during the hypersoft (shown in black) and the very high (shown in red) state. Two separate structures in the HID of VHS at different count rates are due to the peak and dip phase count rates of the binary orbital motion in the presence of a data gap. To compare with the HID from Koljonen et al. (2010), we put the HID of the FSXR (shown in blue). The relative position of the FSXR and the hypersoft state are similar to that from Koljonen et al. (2010), but a new state (very high state) is found between them with the *AstroSat* observation that coincides with the jet line proposed by Koljonen et al. (2010).

law to the radio frequency should indicate the expected radio flux density. To check the consistency, we consider the LAXPC spectrum of the VHS in 25–70 keV and fit it with a power law. Such a choice of energy range ensures that no other model components contribute significantly in this band. The fitted spectrum and its residual are shown in the top and middle panels of Figure 4. The best-fit power-law index and power-law normalization are $1.49^{+0.04}_{-0.03}$ and $0.065^{+0.006}_{-0.005}$, respectively. Both parameters are consistent with those from the power-law model used during the broadband spectral fitting of VHS (see Table 1). When we extrapolate the fitted power-law model to the radio band, shown in the bottom panel of Figure 4, we find that the radio flux density predicted by the X-ray power-law model is in the range of ∼185–511 mJy at 11.2 GHz. The radio flux density observed by the RATAN-600 radio telescope at 11.2 GHz is 40 ± 2 mJy on MJD 57845.23 and 1650 ± 70 mJy on MJD 57846.21. The VHS spectrum analyzed here was observed between MJD 57845.34 and 57845.69. Therefore, our observations lie exactly between two radio observations, and the X-ray spectral model fit predicted radio flux density is highly consistent with the trend shown in the top left panel of Figure 1.

4. Summary and Conclusions

In this work, we jointly analyze observations of Cyg X-3 using simultaneous SXT and LAXPC data on board *AstroSat* on 2017 April 1–2 when the formation of a giant radio flare was reported using the RATAN-600 radio telescope.

During the first half of the *AstroSat* observation (∼0–50 ks), the X-ray spectra are unusually soft, and the source is not detected significantly above 20 keV. This is consistent with the HPS that was previously observed a few times from Cyg X-3 (Koljonen et al. 2010). The hardness ratio during the HPS is lower when compared to the FSXR state with no significant counts above 20 keV. During the second half of the observation (∼60–93 ks), the 20–60 keV count rate increases by a factor of ∼5–6 and the hardness ratio also increases by ∼50%. This makes source spectral state different than that observed during the first half of the observation. Comparing with the FSXR, we

Table 1
Best-fit Parameters Using SXT and LAXPC Joint Spectral Fitting during the Hypersoft and the Very High State

Model	Parameters	Hypersoft State	Very High State
tbabs	$N_{H,ISM}$ (10^{22} cm^{-2})	$3.17^{+0.04}_{-0.05}$	$3.63^{+0.04}_{-0.03}$
pcfabs	$N_{H,loc}$ (10^{22} cm^{-2})	$13.5^{+0.5}_{-0.6}$	$14.1^{+0.4}_{-0.5}$
	f_{sc}	$0.65^{+0.02}_{-0.01}$	$0.71^{+0.02}_{-0.02}$
diskbb	kT_{in} (keV)	$1.39^{+0.03}_{-0.02}$	$1.11^{+0.03}_{-0.02}$
	$\sqrt{N_{dbb}}$	$16.4^{+3.1}_{-2.6}$	$31.8^{+2.1}_{-4.4}$
bremss	kT_{plasma} (keV)	$4.58^{+0.42}_{-0.31}$	$3.87^{+0.19}_{-0.16}$
	N_{bremss}	$0.59^{+0.21}_{-0.18}$	$3.62^{+0.62}_{-0.53}$
powerlaw	Γ	⋯	$1.43^{+0.06}_{-0.03}$
	$N_{powerlaw}$	⋯	$0.04^{+0.01}_{-0.01}$
gauss	E_{Gauss} (keV)	$6.94^{+0.04}_{-0.03}$	$7.08^{+0.04}_{-0.12}$
	W_{eq} (eV)	96^{+11}_{-8}	59^{+5}_{-3}
gabs	E_{gabs} (keV)	$2.96^{+0.01}_{-0.01}$	$2.95^{+0.01}_{-0.02}$
	σ_{gabs} (keV)	$0.07^{+0.01}_{-0.01}$	$0.06^{+0.02}_{-0.01}$
	Depth$_{gabs}$ (keV)	$0.04^{+0.01}_{-0.01}$	$0.03^{+0.01}_{-0.01}$
$F_{0.3-3}$	(10^{-10} erg s^{-1} cm^{-2})	$8.68^{+0.22}_{-0.43}$	$13.6^{+0.64}_{-0.62}$
F_{3-6}	(10^{-10} erg s^{-1} cm^{-2})	$53.4^{+1.29}_{-1.55}$	$55.8^{+1.69}_{-1.43}$
F_{6-10}	(10^{-10} erg s^{-1} cm^{-2})	$15.8^{+1.13}_{-0.56}$	$28.7^{+1.14}_{-1.15}$
F_{10-20}	(10^{-10} erg s^{-1} cm^{-2})	$2.32^{+0.13}_{-0.09}$	$7.91^{+1.09}_{-1.17}$
F_{20-80}	(10^{-10} erg s^{-1} cm^{-2})	$0.35^{+0.12}_{-0.24}$	$9.43^{+3.17}_{-2.32}$
χ^2/dof		981/708 (1.39)	1221/854 (1.43)

Note. $N_{H,ISM}$ and $N_{H,loc}$ are the line of sight, interstellar medium, and local absorption column density, respectively; f_{sc} is the scattering fraction; and kT_{in} and N_{dbb} are the inner disk temperature and diskbb normalization, respectively. Γ and $N_{powerlaw}$ are the photon power-law index and the power-law normalization. kT_{plasma} and N_{bremss} are plasma temperature and the bremss normalization. E_{Gauss} and W_{eq} are the Fe emission line energy and the equivalent width, respectively. E_{gabs} and σ_{gabs} are the energy and width of the Gaussian absorption line in keV while Depth$_{gabs}$ is the line depth. $F_{0.3-3}$, F_{3-6}, F_{6-10}, F_{10-20}, and F_{20-80} are fluxes in the energy ranges 0.3–3, 3–6, 6–10, 10–20, and 20–80 keV, respectively.

show that the second half of *AstroSat* observation falls between the HPS and the FSXR and we termed this here as the VHS. Interestingly, if we qualitatively compare our HID with
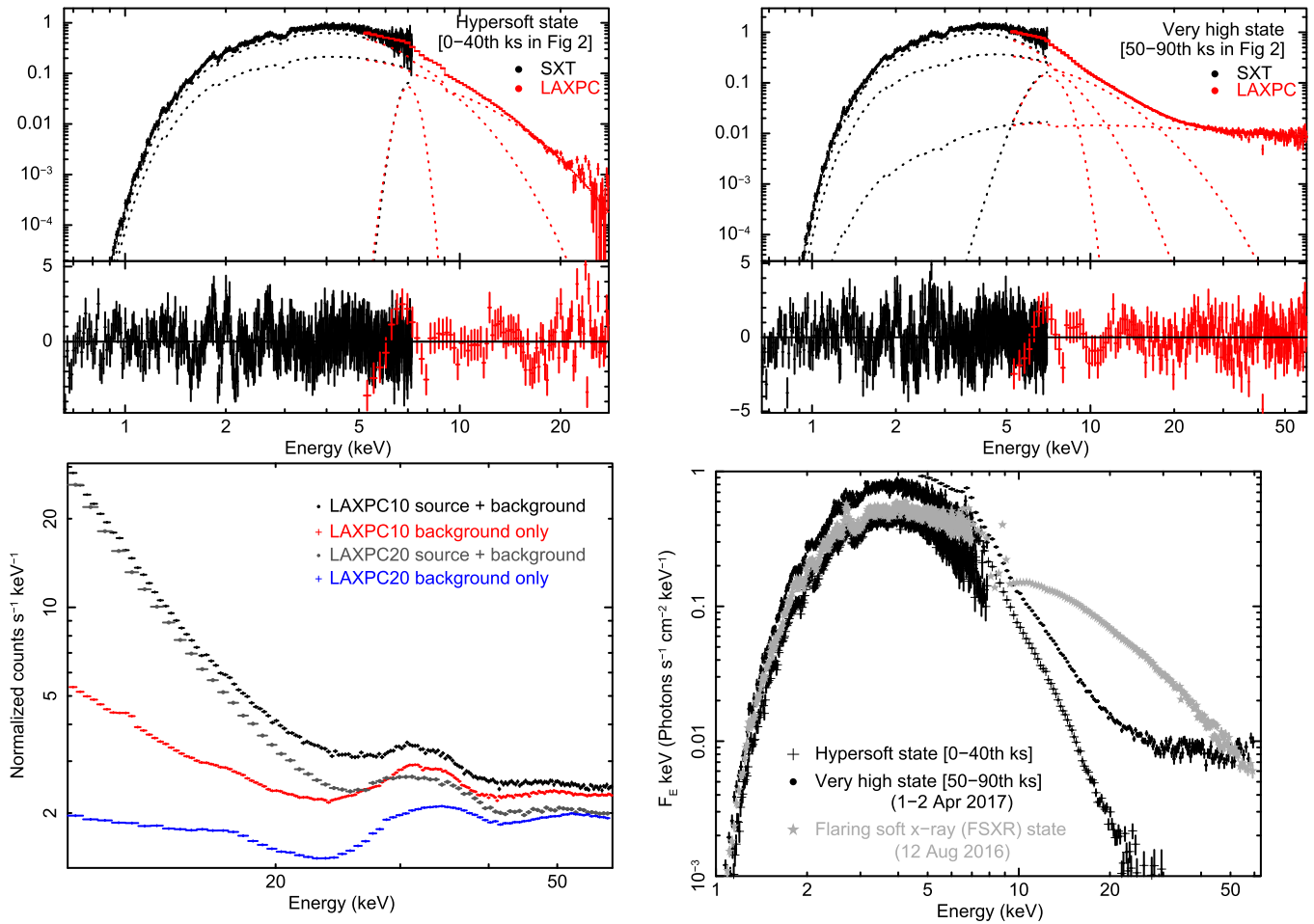
Figure 3. Top left and top right panels show the best-fit joint spectra from SXT (black) and LAXPC (red) during the hypersoft and the very high states, respectively, along with the fitted model components and residuals. Bottom left panel shows the LAXPC10 and LAXPC20 source+background and background spectra simultaneously in 10–60 keV during the very high state. Due to the gain instability issue caused by a minor gas leakage, LAXPC30 spectra are excluded (Antia et al. 2017). Bottom right panel shows the best-fit unfolded spectrum during the hypersoft (shown by pluses) and very high state (shown by circles). To compare these spectra with the flaring soft X-ray state (FSXR), we show the unfolded FSXR spectrum (shown in gray) that was observed on 2016 August 12 with *AstroSat*.

Figure 3 from Koljonen et al. (2010), we notice that the jet line that divides the HPS from FSXR in Koljonen et al. (2010) coincides with the position of the VHS as observed by the *AstroSat*. Therefore, using *AstroSat* observations, we classify VHS as an additional state that falls between the HPS and FSXR state in the HID.

An indication that the significant hard X-ray emission (>15 keV) during the VHS originates from a physical process different than the disk blackbody comes from a significantly low SRCC (0.17) between the 3–6 keV and 15–60 keV count rates, while the same during the HPS is very high (0.82). The spectral modeling of the hard X-ray excess during the VHS indicates a power-law index of ~1.49. The extrapolated power-law model predicts the radio flux density in the range of ~185–511 mJy, consistent with the trend observed from the RATAN-600 telescope at 11.2 GHz. Comparing with the contemporary radio flux we conclude that such a flat X-ray power-law emission is solely due to the synchrotron emission from the slowly moving jet base. The radio flare rise time is slower in Cyg X-3 (Trushkin et al. 2017b) in comparison to the rise time seen in GRS 1915

+105 (Yadav 2006), which is consistent with the slower speed of superluminal radio jets in Cyg X-3 (Marti et al. 2000). The detection of hard X-ray emission from radio jets in GRS 1915+105 may be difficult since accretion disk emission is stronger in GRS 1915+105 and superluminal radio jets in GRS 1915+105 are weaker at least by a factor of over ~20 (Yadav 2006).

From Table 1, we note that during the HPS to the VHS transition, the inner disk temperature decreases from ~1.39 keV to ~1.11 keV, while the inner disk radius (which is proportional to the square root of diskbb normalization) increases by a factor of ~2. This implies the inner disk recedes during the formation of a major plasma blob that emits a radio flare. A significant increase in the contribution of the bremsstrahlung emission from ~13% (during HPS) to ~36% (during VHS) of the total flux in 0.1–100.0 keV along with appearance of the hard X-ray tail implies that the plasma blob, in the presence of a strong magnetic field, is capable of emitting synchrotron radiation in radio frequency, and we detect the high-energy part of such radiation as a flat power-law component in the X-ray spectra.
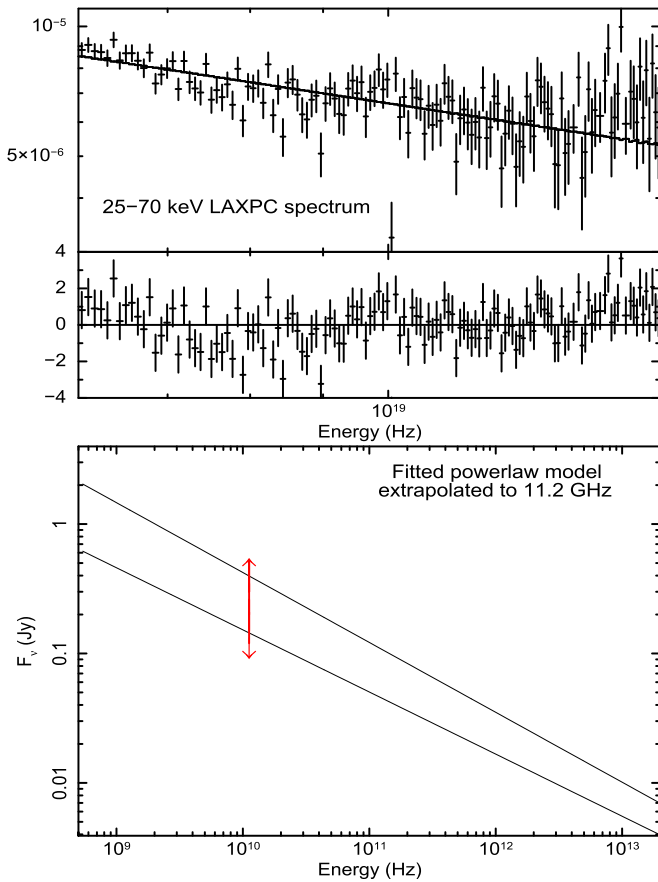
Figure 4. Top and middle panels show 25–70 keV LAXPC spectra fitted with a power law during the very high state and its residual, respectively. The bottom panel shows the best-fit power-law model when extrapolated to radio frequencies. Two black lines are models corresponding to the 2σ upper and lower limits of power-law indices, respectively. The vertical red line segment shows the range between two radio flux density measurements at 11.2 GHz during the X-ray observation of VHS.

ORCID iDs

Mayukh Pahari ⓘ https://orcid.org/0000-0002-5900-9785
Jai Verdhan Chauhan ⓘ https://orcid.org/0000-0002-5736-1654
Sunil Chandra ⓘ https://orcid.org/0000-0002-8776-1835
Sudip Bhattacharyya ⓘ https://orcid.org/0000-0002-6351-5808

References

Agrawal, P. C., Yadav, J. S., Antia, H. M., et al. 2017, JApA, 38, 30
Antia, H. M., Yadav, J. S., Agrawal, P. C., et al. 2017, ApJS, 231, 10
Beckmann, V., Soldi, S., Beĺanger, G., et al. 2007, A&A, 473, 903
Casella, P., Belloni, T., & Stella, L. 2005, ApJ, 629, 403
Corbel, S., Coriat, M., Brocksopp, C., et al. 2013, MNRAS, 428, 2500
Dinçer, T., Kalemci, E., Tomsick, J. A., Buxton, M. M., & Bailyn, C. D. 2014, ApJ, 795, 74
Fender, R., & Belloni, T. 2004, ARA&A, 42, 317
Fender, R. P., Belloni, T. E., & Gallo, E. 2004, MNRAS, 355, 1105
Fender, R. P., Homan, J., & Belloni, T. M. 2009, MNRAS, 396, 1370
Koljonen, K. I. I., Hannikainen, D. C., & McCollough, M. L. 2011, MNRAS, 416, L84
Koljonen, K. I. I., Hannikainen, D. C., McCollough, M. L., Pooley, G. G., & Trushkin, S. A. 2010, MNRAS, 406, 307
Koljonen, K. I. I., Maccarone, T., McCollough, M. L., et al. 2017, A&A, in press (arXiv:1712.07933)
Koljonen, K. I. I., McCollough, M. L., Hannikainen, D. C., & Droulans, R. 2013, MNRAS, 429, 1173
Leach, R. W., Murray, S. S., Schreier, E. J., et al. 1975, ApJ, 199, 184
Manchanda, R. K. 2002, JApA, 23, 197
Manchanda, R. K., & Rao, A. R. 1993, AdSpR, 13, 335
Marti, J., Paredes, J. M., & Peracaula, M. 2000, ApJ, 545, 939
Miller-Jones, J. C. A., Sivakoff, G. R., Altamirano, D., et al. 2012, MNRAS, 421, 468
Mioduszewski, A. J., Rupen, M. P., Hjellming, R. M., et al. 2001, ApJ, 553, 766
Misra, R., Yadav, J. S., Verdhan Chauhan, J., et al. 2016, ApJ, 835, 195
Molnar, L. A., Reid, M. J., & Grindlay, J. E. 1988, ApJ, 331, 494
Muno, M. P., Remillard, R. A., Morgan, E. H., et al. 2001, ApJ, 556, 515
Pahari, M., Antia, H. M., Yadav, J. S., et al. 2017, ApJ, 849, 16
Parsignault, D. R., Gursky, H., Kellogg, E. M., et al. 1972, NPhS, 239, 123
Schalinski, C. J., Johnston, K. J., Witzel, A., et al. 1995, ApJ, 447, 752
Singh, K. P., Tandon, S. N., Agrawal, P. C., et al. 2014, Proc. SPIE, 9144, 91441S
Stirling, A. M., Spencer, R. E., de la Force, C. J., et al. 2001, MNRAS, 327, 1273
Trushkin, S. A., McCollough, M., Nizhelskij, N. A., & Tsybulev, P. 2017a, Galax, 5, 86
Trushkin, S. A., Nizhelskij, N. A., Tsybulev, P. G., & Zhekanis, G. V. 2017b, ATel, 10126
Yadav, J. S. 2006, ApJ, 646, 385
Yadav, J. S., Agrawal, P. C., Antia, H. M., et al. 2016a, Proc. SPIE, 9905, 99051D
Yadav, J. S., Misra, R., Verdhan Chauhan, J., et al. 2016b, ApJ, 833, 27
Zdziarski, A. A., Misra, R., & Gierliński, M. 2010, MNRAS, 402, 767
Zdziarski, A. A., Segreto, A., & Pooley, G. G. 2016, MNRAS, 456, 775